Inflammation modulates lymph node biomechanics in a sex-dependent manner

Ann Ramirez[1 #], Vedanth Sriram[1,2 #], Yassmin Abbouchi[1], Reina Patolia[1], Emily Passaro[1], Michele Kaluzienski[1], Katharina Maisel[1,2*]

Affiliations:

1: Fischell Department of Bioengineering, University of Maryland, College Park

2: Biophysics Program, University of Maryland, College Park

#Authors contributed equally to the manuscript

*** Correspondence to:**

Dr. Katharina Maisel

Fischell Department of Bioengineering

University of Maryland, College Park

Email: maiselka@umd.edu

ABSTRACT

Lymph nodes are highly specialized immune organs that orchestrate the adaptive immune response. In the lymph nodes, naïve B and T lymphocytes encounter cognate antigens, sparking their activation and response to foreign substances. Lymph nodes grow in response to an immune challenge, at least in part to accommodate increased numbers of infiltrating and proliferating B and T lymphocytes. This behavior is supported by a robust three-dimensional network of extracellular matrix (ECM) fibers and fibroblastic reticular cells (FRCs). ECM fibers and FRCs work synergistically to alternate stretching and contractile forces between them allowing the lymph node to maintain structural integrity during rapid tissue reconstruction. These changes ultimately alter the material properties of the lymph node, which can impact cell migration, proliferation, and differentiation. Recent work has investigated the physiological implications of the changing lymph node microenvironment; however, the biophysical properties of the lymph nodes during these changes remain largely unexplored. Here, we use multiple particle tracking microrheology (MPT), a minimally invasive nanoparticle-based technique to investigate the biophysical properties (elastic/loss moduli, microviscosity, pore size) of lymph nodes post inflammatory stimulus. Our results highlight mechanical changes both during the initial phases of the acute inflammatory response and upon resolution of inflammation, a topic that is relatively understudied. We show that B and T cell rich areas restructure independently, with T cell zones remodeling significantly and exhibiting nearly a 3-fold higher elastic modulus. Additionally, for the first time, we show that biological sex modulates lymph node biomechanics in acute inflammation: Lymph nodes from female mice showed a ~20-fold increase in elastic and loss moduli at peak inflammation, while lymph nodes from male mice had a ~5-fold decrease in both moduli. Additionally, lymph nodes from female mice appeared to permanently remodel during the resolution of acute inflammation

resulting in the maintenance of an overall higher elastic and loss modulus, while lymph nodes from male mice returned to the biomechanics of untreated lymph nodes. We also found that at least some of the changes in biomechanical properties were correlated with changes in ECM materials in the lymph nodes, suggesting a structure-function relationship. Overall, our studies provide key insights into how biomechanical properties in lymph nodes are altered during inflammation, a previously unstudied area, and lay the foundation for structure-function relationships involved in immune response. Additionally, we demonstrate a robust technique for the analysis of the lymph node interstitial tissue properties and how they vary with inflammatory stimuli.

INTRODUCTION

The lymph node is key in shaping the adaptive immune response. The complex coordination of adaptive immune cell (lymphocyte)-mediated immune responses is largely due to the lymph node's highly organized structure. The lymph node can be separated into three distinct regions: the cortex, paracortex, and medulla. The T cell response, the cell-mediated arm of adaptive immunity that results in direct killing of, e.g., infected or cancerous cells, is coordinated in the paracortex. The B cell response, our humoral or antibody-mediated immunity, is coordinated in the cortex. Lymph fluid travelling from peripheral tissues to the lymph nodes flows around the lymph node and into the inner medulla as well as into the subcapsular sinus, and into the cortex and paracortex. Macrophages that line the subcapsular sinuses break down larger materials into smaller antigens to be released into the cortex or paracortex to stimulate T and B cell responses, and small materials <100 kDa in size enter the cortex and paracortex via the conduit system[1]. The conduit system, also called the reticular network, is made up of fibroblastic reticular cells (FRCs) that ensheath a network of collagen fibers that build a key structural component within the lymph node. FRCs maintain these fibers and produce additional collagen during lymph node expansion and contraction that occur during immune responses[2,3]. Other non-lymphocytes, including fibroblasts, blood and lymphatic endothelial cells, as well as macrophages also contribute to changes in the lymph node structure during inflammation and as we age.

During inflammatory processes, the lymph node undergoes significant structural changes. Within a few hours of an immune insult, whether a bacterial infection due to a cut or the onset of a flu infection, a massive influx of migrating lymphocytes and antigen presenting cells, including dendritic cells (DCs) coming from the injured tissue, enter the lymph node. At the same time, activated B and T cells and stromal cells (FRCs and lymphatic and blood endothelial cells) begin

proliferating[4,5]. During this initial phase, migratory DCs cause FRCs to relax and retract from, or let go of, the collagen fibers, such that the collagen fibers bear most of the tension due to expansion in size, and it is thought that the mesh spacing within the reticular network is increased[7-10]. As the lymph node continues to expand, breaks occur in the collagen fibers and other extracellular matrix (ECM) materials, requiring repair and transfer of some of the tension to the FRCs themselves[11]. Researchers have found permanent changes after the immune response is resolved and the tissue is again at homeostasis because the outer capsule of the lymph node is thicker and stiffer[9].

Research has shown that the biomechanics, or tension and relaxation that also occur during inflammation in the lymph nodes, can affect cell functions. The FRCs and collagen fibers are hypothesized to provide a structural scaffold for B and T cells that regulates their proliferation and migration, and also to distribute chemokines, cytokines, and growth factors throughout the lymph node[12-15]. T cells respond to their environment by sensing and adapting to the biomechanics, including fluid-like viscous and solid-like elastic stresses. Recently, researchers demonstrated that T cells have higher expression of activation and inhibitory markers when exposed to slow relaxing, more solid-like matrices, while T cells on fast relaxing, more fluid-like matrices had higher expression of memory markers[16]. Biomechanics and viscoelasticity, the combined solid- and fluid-like responses of a tissue, are largely dependent on ECM composition[19]. As we age, we accumulate ECM materials in the lymph nodes (also known as fibrosis), and research has shown that the motility of naïve T cells (circulating T cells prior to exposure to inflammatory stimuli) is decreased in aged compared to young lymph nodes[17]. This is particularly evident near highly ECM-rich fibrotic regions, which are likely to have increased solid-like elastic properties[17]. Aging also appears to modulate naïve T cell numbers, which suggests that fibrosis and biomechanical properties of the lymph nodes could be a contributing factor to age-related changes in our adaptive

immune response [18]. Interestingly, ECM composition and biomechanics of tissues is sex-dimorphic in many organs[20-22] and these differences may be a contributing factor to sex differences in susceptibility and progression of numerous diseases[20,23].

Despite the importance of ECM and viscoelasticity in the context of lymphocyte immunity, lymph node biomechanics and viscoelasticity have yet to be examined extensively, including in the context of inflammation. This is in part due to limitations to the methods available to study viscoelastic properties, traditionally via rheology[24] or atomic force microscopy[25,26]. A rheometer applies a shear or linear stress with a known displacement or speed on the sample and the resulting torque (or stress) the material responds with is recorded. While this is a satisfactory method for homogeneous substances, it is inadequate for samples like the lymph node since the spatial organization vital to its various functions is lost. Additionally, the rheometer usually requires a larger volume than what is available from smaller organs like the lymph nodes. Atomic force microscopy uses a cantilever that touches a sample surface at a constant force. The surface topography causes deflections in the cantilever, which alters the amount of laser light reflected from its surface and captured by a photodetector[25,26]. This readout can be used to infer the sample's viscoelastic response. While this method preserves the spatial organization of tissues, the analysis is limited to the sample surface and is sacrificial, making it less than ideal for studies aiming to look at both structure and function. Researchers have also used more specific methods, including tension nanoprobes to study lymph node elasticity[27], tensiometers to study capsule rigidity[28], 2-photon microscopy to study lymph node fibrosis[17], and nanoindentors to test lymph node viscoelasticity[9,29]. These methods have been helpful in elucidating lymph node biomechanics, but none of these are non-sacrificial nor provide biomechanical properties beyond the surface.

We have previously pioneered combining nanoparticle-based multiple particle tracking

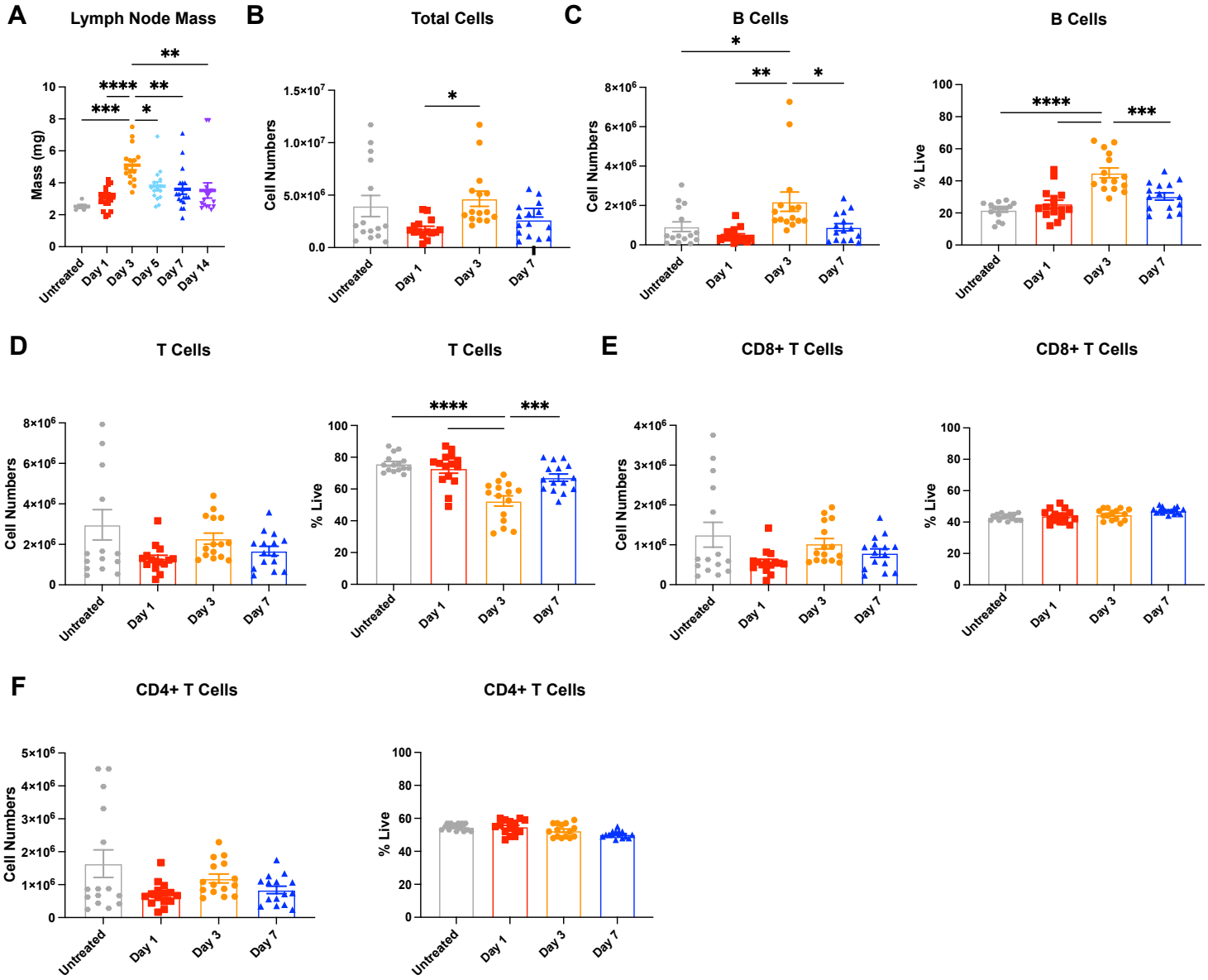

Figure 1. Lymph nodes (LNs) expand and contract over 14 days post single stimulation with lipopolysaccharide (LPS). (A) Mass of inguinal lymph node. (B) Total cell, (C) B cell (CD45+B220+), and (D) T cell (CD45+CD3+) numbers in lymph nodes collected by flow cytometry. (E) CD8+T cell (CD45+CD3+CD8+) and (F) CD4+ T cell (CD45+CD3+CD4+) numbers in lymph nodes collected by flow cytometry 1-, 3-, and 7-days post LPS stimulus. All values are reported as mean ± SEM. Statistical analysis performed by one-way ANOVA followed by Tukey's post-hoc test **(A-F)**. *p<0.05, **p<0.01, ***p<0.001, ****p<0.0001. N=10-15 female mice per group.

(MPT) microrheology[30,31] with live lymph node slice culture, which allows us to preserves tissue architecture ex vivo[32] while simultaneously studying lymph node viscoelasticity[30]. MPT uses nanoparticles of sizes close to, but smaller than, the mesh spacing of hydrogel-like tissues and tracks their Brownian diffusive motion within the tissue over time. The resulting mean-squared displacement for each particle and the ensemble of all particles is then used to determine biomechanical properties such as elastic and loss modulus, pore size, and microviscosity of the lymph nodes[30,33-36]. Here, we investigate how the biomechanics of the lymph node change during inflammation, particularly in the cortex and paracortex (B and T cell zones). We correlate our microrheology measurements to structural changes in lymph node ECM and assess differences in biomechanical responses to inflammation based on sex. Our study presents, for the first time, an in-depth analysis of the complex biomechanics of distinct lymph node regions during an inflammatory response in the context of tissue remodeling and sex, and lays the foundation for future structure-function relationships between tissue biomechanics and lymphocyte functions.

RESULTS

LPS induces peak inflammation in lymph nodes at day 3 and returns to homeostasis by day 14

We inflamed the lymph nodes via intradermal injections of 10 μg lipopolysaccharide (LPS) in female mice to simulate a bacterial challenge. After a single LPS challenge, lymph node mass peaked on day 3 to nearly two-fold compared to untreated mice, started to decrease by day 5 ($p<0.1$), and returned to masses similar to untreated by day 7 (**Fig. 1A**). We found that cell numbers in the lymph nodes first decreased from 4 ± 1 million in untreated to 1.8 ± 0.2 million in day 1 lymph nodes, followed by a significant increase to 4.7 ± 0.7 million on day 3 (**Fig. 1B**). B cells significantly contributed to this increase (**Fig. 1C**), as they increased in number from 0.9 ± 0.2

million cells in untreated to 2.2 ± 0.5 million cells in day 3 lymph nodes (**Fig. 1C**). B cell numbers returned close to values for untreated mice by day 7. While not significantly different, we observed that CD8+ and CD4+ T cell numbers also appeared to contract at day 1 and expand again on day 3 (**Fig. 1D-F**).

Peak inflammation increases biomechanical properties of the lymph nodes while reducing pore size

We used multiple particle tracking (MPT) to assess lymph node biomechanical properties, including elastic and loss moduli, pore size, and microviscosity. After performing MPT, the nanoparticles' mean squared displacement that occurs due to their Brownian motion in the lymph node tissues can be used to extrapolate these various properties, and tissues typically exhibit both elastic and viscous properties. The elastic modulus describes the solid-like properties of a material and refers to how well it returns to its original shape after a force is applied (**Fig. 2A**). The loss modulus describes the liquid-like properties of a material, or the viscous response, that permanently deforms the sample (**Fig. 2A**). We used collagen III and B220 staining to delineate B and T cell zones in the lymph nodes (**Fig. 2B**). We found that 500 nm nanoparticles freely diffuse through the lymph node microenvironment, suggesting that this is the optimal size to probe the 'mesh' components, including cells and ECM, as well as fluid components, including interstitial fluid (**Supp. Fig. S1**). We observed a significant increase in lymph node microviscosity during early stages of inflammation, with the overall viscosity reaching a peak value of 3.5 ± 1.2 Pa*s on day 3 (**Fig. 2C)**. Lymph nodes had a significantly higher elastic modulus of 2.2 ± 0.7 Pa on day 3, indicating a stiffer lymph node, compared to all other days (**Fig. 2D, 2E**). Lymph nodes begin to return to elastic modulus values close to healthy by day 7 (0.2 ± 0.06 Pa) (**Fig. 2D-E**). We also observed a significant increase in loss modulus on day 3, 1.9 ± 0.6 Pa, compared to untreated, 0.07

± 0.02 Pa, which indicates a high resistance to fluid flow at peak inflammation (**Fig. 2D-E**). We found a significant increase in median pore size on day 1 of 1400 nm compared to 800 nm in untreated lymph nodes, indicating tissue relaxation at the start of the inflammatory response (**Fig. 2F**). Pore size then decreased significantly to 270 nm on day 3 (**Fig. 2F**) and began to increase again thereafter. Our data support prior work suggesting that lymph nodes initially relax to prepare for cell influx and expansion followed by stiffening that occurs after cell influx and proliferation have begun.

To understand underlying causes for changes in pore size, we semi-quantitatively assessed the key ECM component in the lymph node, collagen III, via fluorescence microscopy (**Fig. 2G**). We used either 10µm (obtained via cryostat) or 300µm (obtained via vibratome) thick lymph node sections. In the thicker vibratome slices, we found a significant increase in collagen III mean fluorescent intensity (MFI) from 98 ± 6 AFU in untreated to 640 ± 180 AFU on day 3 (**Fig. 2H**). This data suggests that increases in collagen density may contribute to the decreased pore size observed on day 3 (**Fig. 2F**). In addition, using thin, 10µm lymph node slices stained for podoplanin, a marker of FRCs, in conjunction with a MATLAB script, Gap analysis[7], we calculated pore sizes within the reticular network. Gap analysis fits circles of the largest possible diameter into binarized images of stained tissue to identify and measure non-overlapping gap sizes (**Fig. 2I**). The pore sizes obtained using this method showed different trends to those obtained from MPT data: the median pore size reduced slightly from 670 nm in untreated to 660 nm on day 1 and increased again on day 3 to 670 nm (**Fig 2J**). This trend was likely different since, unlike MPT, Gap analysis does not take into consideration presence of the effects due to cells or other non-collagen materials during the analysis of pore size. We also found no differences in collagen MFI in thin sections (**Fig 2K**). These contrasts suggest that the characterization method used can significantly influence the

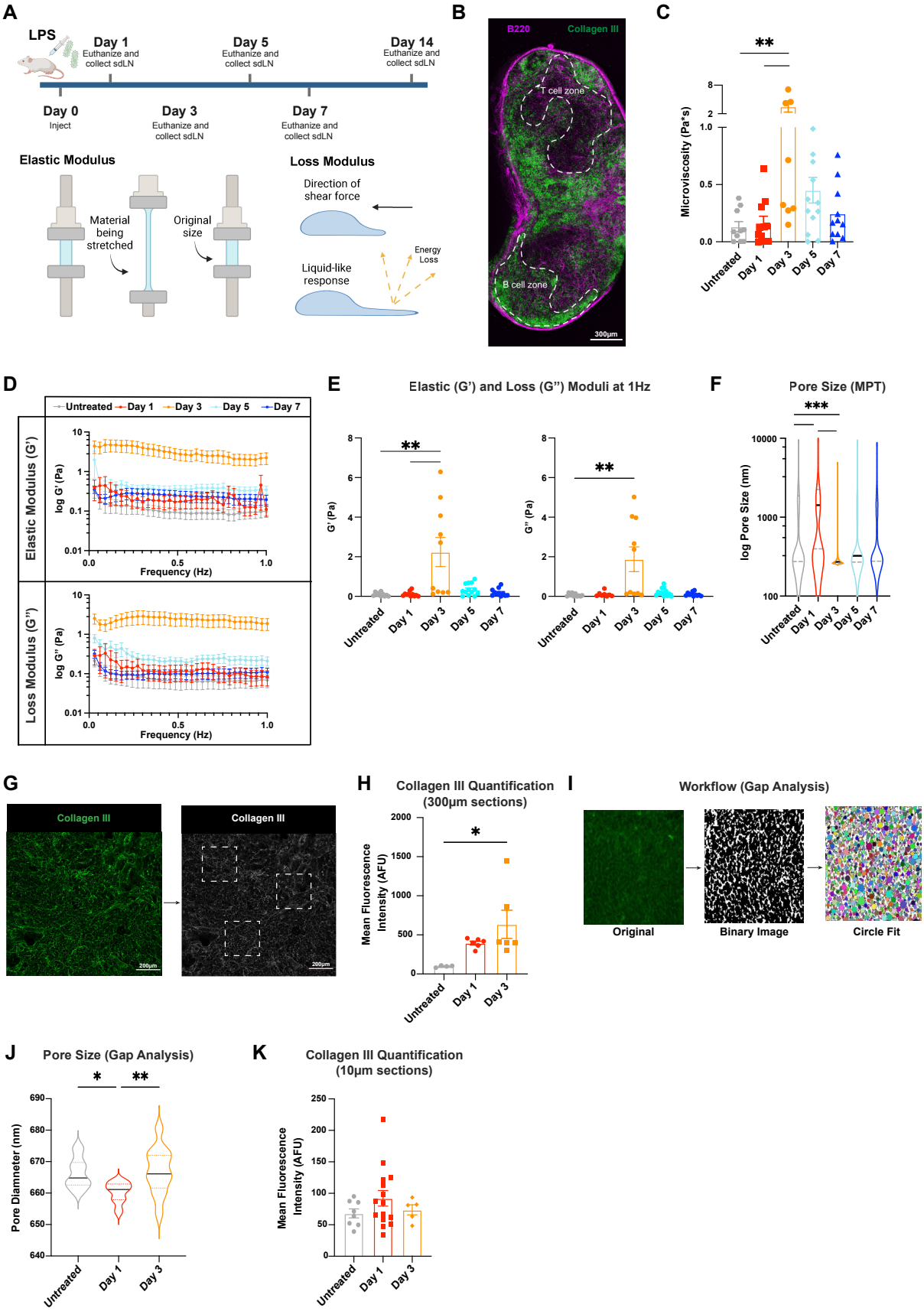

Figure 2 *Lymph node biomechanics change in response to LPS* (A) Injection schedule, schematic of elastic modulus, schematic of loss modulus (made with BioRender). (B) Lymph node slice stained for B220 (B cells) and Collagen III (ECM). (C) Microviscosity of the overall lymph node. (D) Elastic and loss moduli of overall lymph node over 1Hz and (E) at 1Hz. (F) Pore sizes (by MPT) in the overall lymph node. (G) Collagen III quantification workflow and (H) Collagen III quantification from confocal images using tissue slices (300µm thick) obtained using a vibratome. (I) Workflow of gap analysis and (J) pore sizes measured by gap analysis (PDPN staining). (K) Collagen III quantification using tissue slices obtained via cryosectioning (10µm thick). Median and quartile values shown for pore sizes. Other values are reported as mean ± SEM. Y-axis in **D, F** shown on a logarithmic scale, axes labeled with 'log' to enhance readability. Statistical analysis performed with 1-way ANOVA/Kruskal-Wallis tests followed by Tukey's/Dunn's multiple-comparisons post-hoc tests **(C,F,H,J,K)**. Elastic and loss moduli are compared at 1Hz as an average across all mice, and statistical analysis was done using Kruskal-Wallis test with Dunn's post-hoc analysis **(E)**. *p<0.05, **p<0.01, ***p<0.001, ****p<0.0001. N = 10-15 female mice.

information gained regarding the mesh spacing in hydrogel-like tissues.

B and T cell zones restructure independently of each other

B and T cell zones, or cortex and paracortex, in the lymph nodes serve unique functions that lead to B and T cell activation during an inflammatory response. Overall, our data suggest that B and T cell zones have similar microviscosities, with mean values ranging from 0.055 – 2.3 Pa*s for the B cell zone and 0.16 – 3.8 Pa*s for the T cell zone (**Fig. 3A**), with a maximum microviscosity at day 3 in both T and B cell zones. Elastic moduli, in contrast, were generally higher in the T cell zone compared to the B cell zone in untreated mice and on day 3 (**Fig. 3B-C**), suggesting that the two zones restructure differently. We also found that loss moduli are higher in the T cell zone compared to B cell zones in the untreated mice, with 0.12 ± 0.06 Pa compared to 0.03 ± 0.01 Pa, respectively (**Fig. 3B-C**). Loss moduli are similar on day 3, with 1.7 ± 0.1 Pa in the T cell zone and 1.2 ± 0.4 Pa in the B cell zone, and day 7 with 0.1 ± 0.04 Pa in the T cell zone and 0.07 ± 0.03 Pa in the B cell zone (**Fig. 3B-C**).

In both the B and T cell zones, there was an initial increase in pore size. In the B cell zone, median pore size increased from 1300 nm in untreated to 1900 nm on day 1 and then decreased to 280 nm on day 3, followed by an increase to 350 nm on day 5 and 1100 nm on day 7 (**Fig. 3D**). Similarly, the T cell zone median pore size increased from 290 nm in untreated to 1700 nm on day 1 and then decreased to 270 nm on day 3, and remained relatively stable at 320 nm on day 5 and 290 nm on day 7, similar to the pore size of untreated lymph nodes (**Fig. 3D**).

Lymph node biomechanics change permanently after resolution of acute inflammation

Two weeks after inflammation is induced, the overall cell numbers in the lymph node have contracted to 2 ± 0.6 million cells, similar to levels in untreated lymph nodes (4 ± 1 million cells,

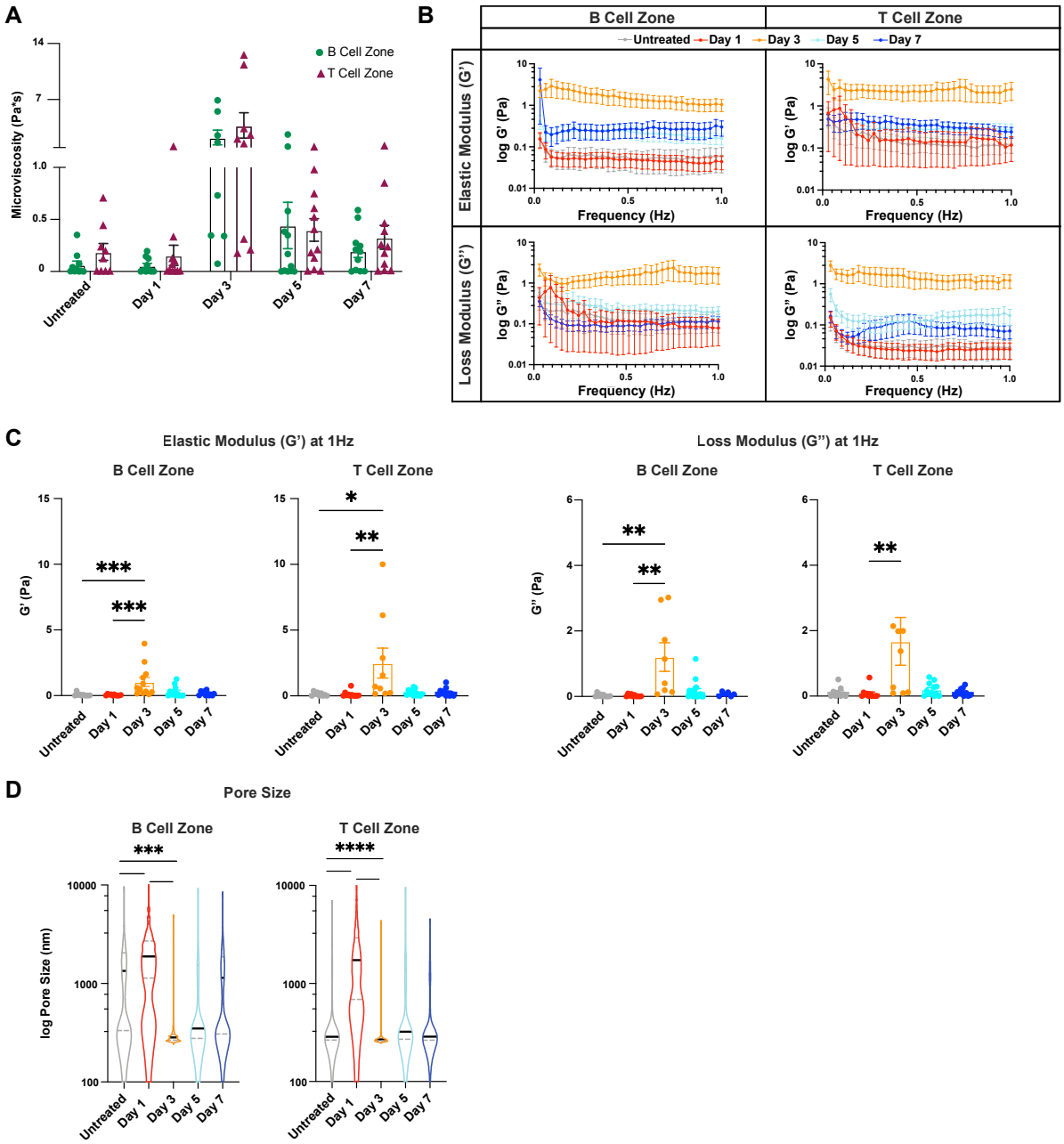

Figure 3 *B and T cell zone biomechanics change independently during immune response to LPS* (A) Microviscosity of the B and T cell zones in untreated lymph nodes and lymph nodes days 1, 3, 5, and 7 after LPS treatment. (B) Elastic and loss moduli of B and T cell zones over 1Hz and (C) at 1Hz. (D) Pore sizes (by MPT) of B and T cell zones during the course of inflammation. Median and quartile values shown for pore sizes. Other values are reported as mean ± SEM. Y-axis in **B, D** shown on a logarithmic scale, axes labeled with 'log' to enhance readability. Statistical analysis of zone-wise comparison of microviscosity was performed using a Mann-Whitney on each day **(A)**, elastic and loss moduli are compared at 1Hz as an average across all mice, and statistical analysis is was performed with a Kruskal-Wallis test with Dunn's post-hoc analysis **(C)**. Statistical analysis for pore size was done using a Kruskal-Wallis test followed by Dunn's post-hoc test **(D)**. *p<0.05, **p<0.01, ***p<0.001, ****p<0.0001. N = 10-15 female mice.

(**Fig. 4A**). Similarly, B cell and T cell numbers (**Fig. 4B**), including CD4+ and CD8+ T cell subsets (**Fig. 4C**), return to levels similar to untreated. These data suggest that at day 14, lymph node cell composition has returned to states similar to untreated, and resolution has occurred. However, we have also found that biomechanical properties of the lymph nodes do not fully return to baseline. Lymph node microviscosity increased 3.5-fold on day 14 compared to untreated (**Fig. 4D**). Though not significantly different, B cell zone microviscosity appeared to be lower than T cell zone viscosity for both untreated and day 14 (**Fig. 4D**). We found a higher elastic modulus, 0.3 ± 0.09 Pa, and loss modulus, 0.2 ± 0.07 Pa, on day 14 compared to 0.1 ± 0.03 Pa and 0.07 ± 0.02 Pa for untreated, respectively, (**Fig. 4E-F**), indicating an overall stiffer tissue that had higher resistance to flow. These data suggest that lymph nodes on day 14 are permanently restructured after a single immune challenge. B cell zones appeared to drive much of these changes, as a greater increase on day 14 was observed for both loss and elastic moduli compared to T cell zones (**Fig. 4E**). We also found a significant decrease in median pore size on day 14 (350 nm) compared to untreated (800 nm) (**Fig. 4G**). We also found an increase in collagen III on day 14 in thick sections compared to untreated **(Fig. 4H).** When assessing pore size based on staining only for the FRC network (podoplanin) using gap analysis, we also found a slight reduction in pore size at day 14 compared to untreated, and thin sections revealed no differences in collagen III **(Fig. 4I-J).** Differences in the values of pore size and collagen quantifications for these two methods are likely due to considering a larger (300 μm MPT/thick sections) or smaller (10 μm gap analysis/cryosections) section of the lymph nodes.

Changes in lymph node biomechanics during inflammation are sexually dimorphic

To determine whether biological sex influences lymph node biomechanics during an acute inflammatory response, we compared the biophysical properties of the lymph nodes between male

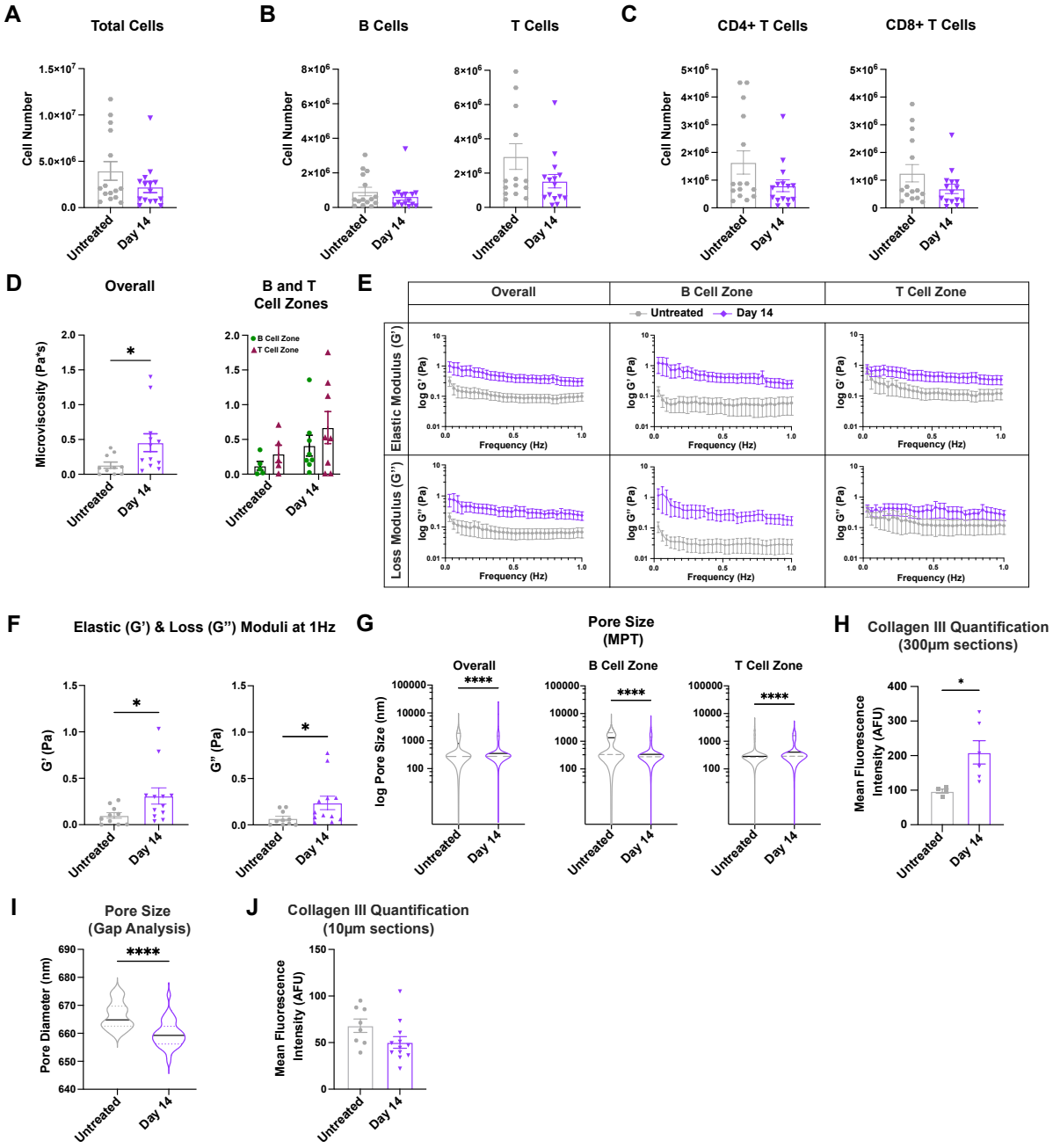

Figure 4 *Lymph node biomechanics show permanent changes at resolution, two weeks after acute inflammatory challenge with LPS* (A) Total cell, (B) B cell (CD45+B220+),T cell (CD45+CD3+), and (C) CD8+ T cell (CD45+CD3+CD8+) and CD4+ T cell (CD45+CD3+CD4+) numbers in lymph nodes from untreated mice and mice 14 days post LPS stimulation analyzed by flow cytometry. (D) Microviscosity in the overall lymph node and in the B and T cell zones from untreated mice and mice 14 days post LPS stimulation. Elastic and loss moduli over (E) 1 Hz and (F) at 1 Hz in the overall lymph node and in the B and T cell zones from untreated mice and mice 14 days post LPS stimulation. (G) Pore sizes (by MPT) in the overall lymph node and in the B and T cell zones. (H) Collagen III quantification from confocal images using tissue slices obtained via vibratome (300µm thick) (I) Pore sizes measured by gap analysis (PDPN staining). (J) Collagen III quantification using tissue slices obtained from a cryostat (10µm thick). Median and quartile values shown in pore sizes. Other values are reported as mean ± SEM. Y-axis in **E, G** shown on a logarithmic scale, axes labeled with 'log' to enhance readability. Statistical analysis performed by a t-test/Mann-Whitney test **(A-D, G, H, I)**. Statistical analysis of zone-wise comparison of microviscosity was performed with a Mann-Whitney test at each timepoint **(D)**. Elastic and loss moduli are compared at 1Hz as an average across all mice, and statistical analysis is done via Mann-Whitney test **(E,F)**. *p<0.05, **p<0.01, ***p<0.001, ****p<0.0001 N = 10-15 female mice.

and female mice at days 3 and 14 post injection, in addition to untreated, to assess differences at peak inflammation and resolution, respectively. We found that female lymph nodes exhibit slightly higher elastic moduli already in untreated states, with 0.11 ± 0.03 Pa in female mice and 0.05 ± 0.004 Pa in male mice (**Fig. 5A-B**), though not significant. At day 3, lymph nodes had significantly higher elastic moduli in female compared to male mice, with 2.2 ± 0.7 Pa vs. 0.01 ± 0.003 Pa, respectively. On day 14, lymph nodes from female mice continued to exhibit higher elastic moduli than those from male mice with 0.3 ± 0.08 Pa vs. 0.05 ± 0.01 Pa (**Fig. 5A-B**), respectively. We found similar results for loss moduli, where the moduli in lymph nodes from female mice were higher compared to those from male mice for both day 3, with 1.9 ± 0.6 Pa (female) vs. 0.005 ± 0.001 Pa (male), and day 14, with 0.23 ± 0.07 Pa (female) vs. 0.02 ± 0.006 Pa (male) (**Fig. 5A-B**). We also found that while elastic moduli and loss moduli reach a peak at day 3 in female mice, they reach a minimum in male mice (**Fig. 5A**). Additionally, we found lower median pore sizes (270 nm vs 1600 nm) (**Fig. 5C**) and higher mean viscosity (3.5 ± 1.1 Pa*s vs. 0.009 ± 0.002 Pa*s) (**Fig. 5D**) on day 3 in lymph nodes from female vs. male mice. Similar trends were observed within the B and T cell zones in lymph nodes of male and female mice at all time points (**Supp. Fig. S2A-C, S3A-B).** When assessing lymph node biomechanics at resolution of inflammation, we found a return to baseline values for both elastic moduli (0.05 ± 0.01 Pa vs. 0.05 ± 0.01 Pa) and loss moduli (0.02 ± 0.005 Pa vs. 0.02 ± 0.006 Pa) in male mice **(Fig 5E)**. However, for female mice, both elastic (0.3 ± 0.08 Pa at day 14 vs. 0.1 ± 0.03 Pa in untreated) and loss moduli (0.23 ± 0.07 Pa at day 14 vs. 0.07 ± 0.02 Pa in untreated) were increased at day 14 (**Fig. 5E**). Independent B and T cell zone restructuring was observed only in lymph nodes from female **(Fig. 4E-F)** mice (**Supp. Fig. S3C).** These data suggest that biological sex influences lymph node restructuring during and after resolution of acute inflammation.

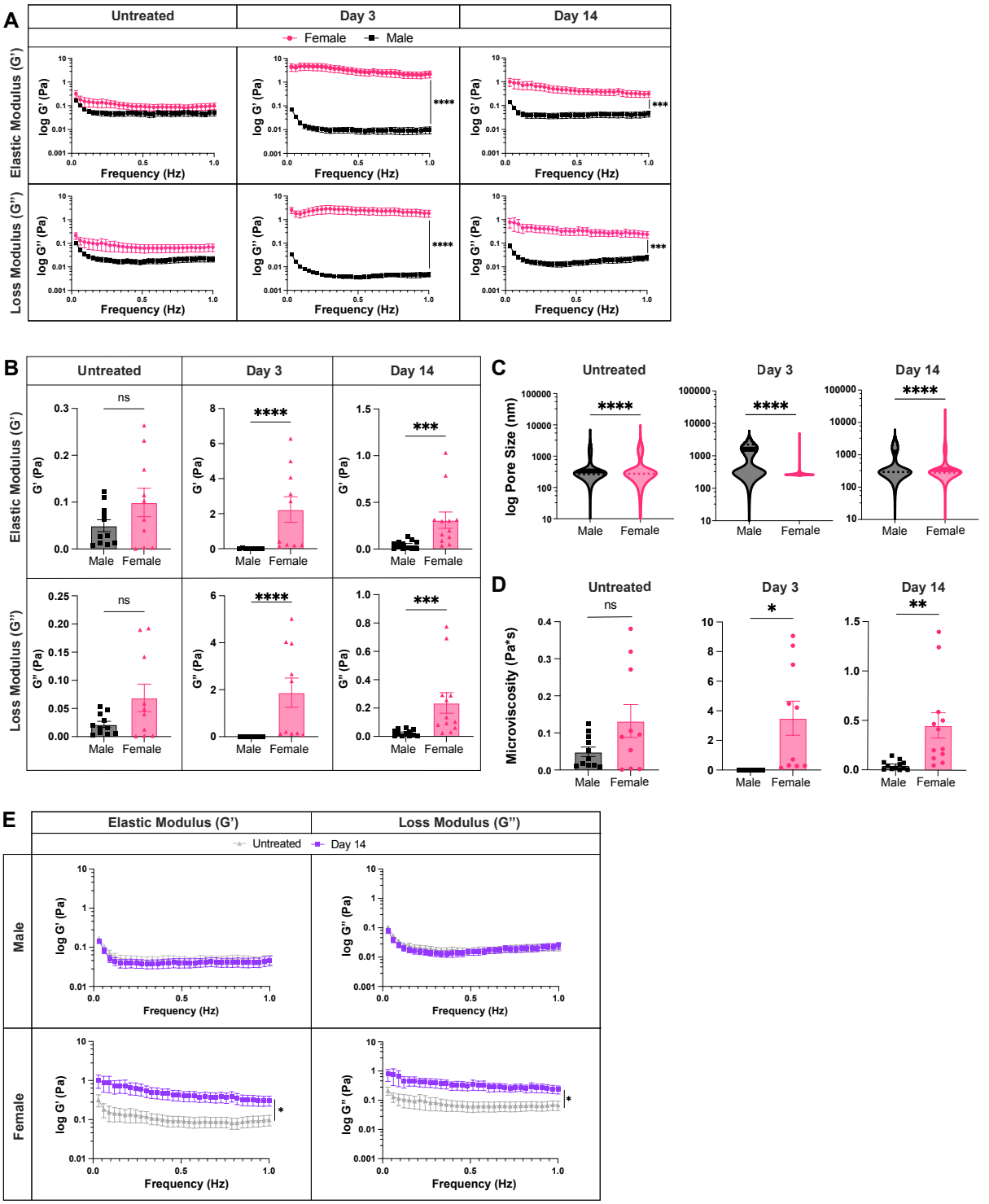

Figure 5. *Lymph node biophysical properties are sexually dimorphic.* Elastic and loss moduli for male and female lymph nodes (A) over 1Hz (B) at 1Hz. (C) Overall pore size (by MPT), and (D) microviscosity of healthy and acutely inflamed male and female lymph nodes. (E) Elastic and loss moduli of male and female lymph nodes for untreated and day 14 lymph nodes over 1Hz. Median and quartile values shown in pore sizes. Other values are mean ± SEM. Y-axis in **A, C, E** shown on a logarithmic scale, axis labelled wivth 'log' to enhance readability. Statistical analysis by Mann-Whitney test (**B,C**) or Welch's t-test (**D**). Elastic and loss moduli are compared at 1Hz as an average across all mice, and statistical analysis is done by t-test/Wilcoxon rank-sum test(**A,B,E**). Significance values are denoted on **A,E** for representation.*p<0.05, **p<0.01, ***p<0.001, ****p<0.0001, ns p≥0.05. N=8-12 male or female mice.

Chronic inflammation does not modulate lymph node biomechanics

Given our findings that acute inflammation induces changes in lymph node biomechanics, we next sought to understand if these changes are enhanced during chronic inflammation. To induce chronic inflammation, 10 μg LPS was intradermally injected weekly for 5 weeks and days 3 and 14 after the final injection were chosen to assess lymph node biomechanics (**Fig. 6A**). Chronically inflamed lymph nodes trended toward more cells on days 3 and 14 (3 ± 0.8 million cells and 2 ± 0.7 million cells, respectively), compared to untreated (0.5 ± 0.09 million cells) (**Fig. 6B**). Compared to untreated (0.1 ± 0.01 million), B cell numbers were increased on day 3 (1 ± 0.4 million) and day 14 (0.6 ± 0.2 million) (**Fig. 6C**). Similarly, there was a trend toward total T cell numbers on day 3 (1.6 ± 0.3 million) and day 14 (1.2 ± 0.4 million) compared to untreated (0.4 ± 0.1 million) (**Fig. 6C**). CD4+ and CD8+ T cell numbers also trended higher on day 3 (0.9 ± 0.2 million and 0.6 ± 0.01 million, respectively) compared to day 14 (0.7 ± 0.2 million and 0.4 ± 0.2 million) (**Fig. 6D**). While the total numbers of total cells, B cells, and T cells were only trending toward significant (p values for all were $p<0.15$), the percent live of each of these was significantly higher at day 3 compared to untreated. By day 14 after the final injection, all cell numbers decreased again and were not significantly different to untreated.

Biomechanical properties of chronically inflamed lymph nodes appeared to be similar 3 days and 14 days after final injection, and remained similar to untreated. Chronically inflamed lymph nodes had microviscosities of 0.1 ± 0.04 Pa*s for untreated, 0.1 ± 0.06 on day 3, and 0.3 ± 0.1 Pa*s on day 14 (**Fig. 6E**). T and B cell zones also had similar microviscosities on day 3 (0.2 ± 0.08 and 0.1 ± 0.05 Pa*s, respectively) and day 14 (both 0.2 ± 0.08 Pa*s) (**Fig. 6E**). Elastic moduli in lymph nodes were also similar on day 3 (0.1 ± 0.05 Pa*s), day 14 (0.2 ± 0.08 Pa*s), and for untreated (0.09 ± 0.03 Pa) (**Fig. 6F**). Elastic moduli were slightly lower on day 3 compared to day 14 in both

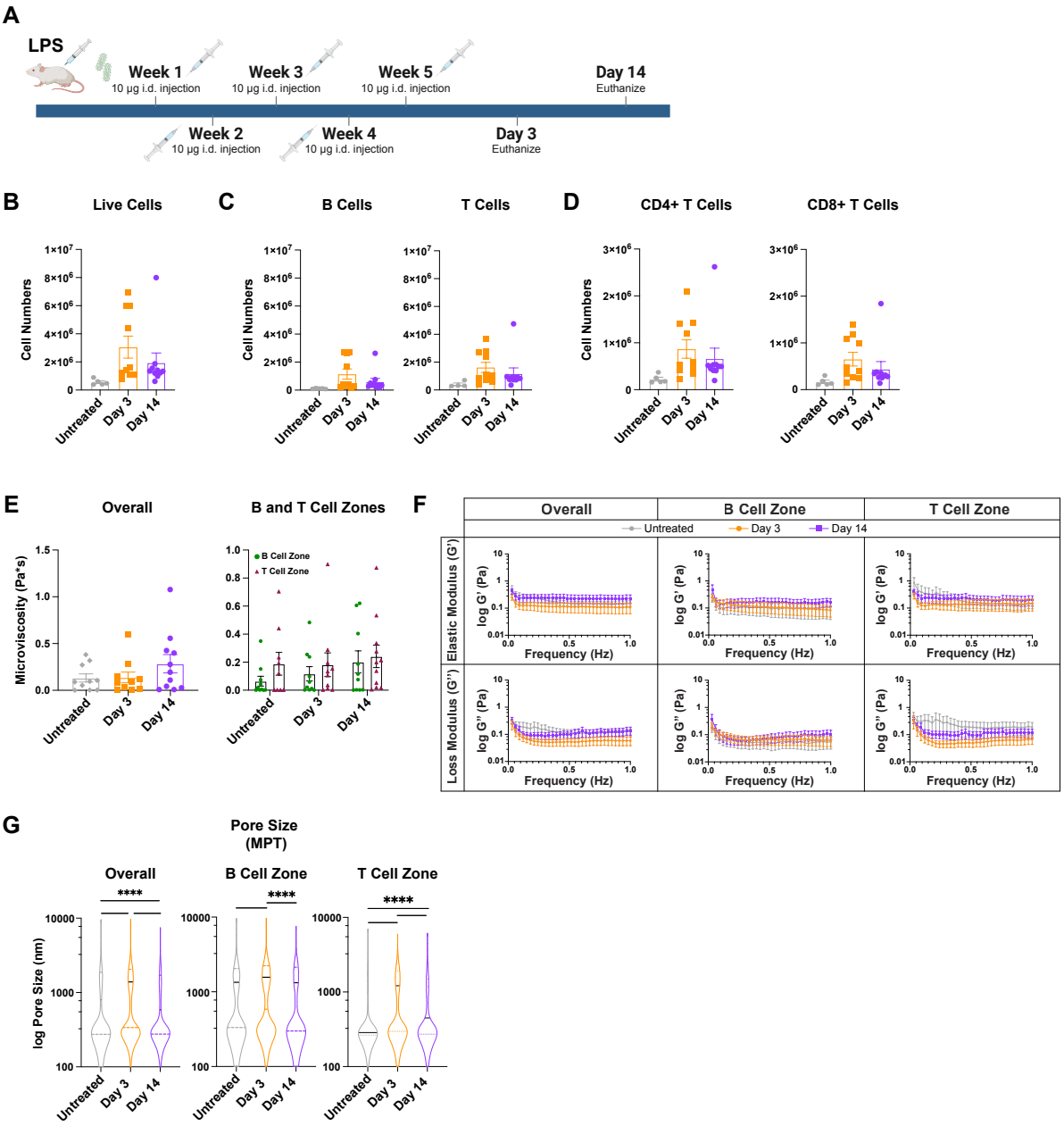

Figure 6 *Chronic inflammation does not modulate lymph node biomechanics* (A) Injection timeline for chronic inflammation studies (B)Total cell, (C) B cell ($CD45^+B220^+$) and T cell ($CD45^+CD3^+$), and (D) CD8+ T cell ($CD45^+CD3^+CD8^+$) and CD4+ T cell ($CD45^+CD3^+CD4^+$) numbers from untreated and chronically inflammed lymph nodes analysed by flow cytometry. (E) Microviscosity (F) elastic and loss modulus over 1 Hz, and (G) pore sizes (by MPT) in the overall lymph node and in the B and T cell zones of untreated chronically inflammed lymph nodes. Median and quartile values shown in pore sizes. Other values are reported as mean ± SEM. Y-axis in **F,G** shown on a logarithmic scale, axis labelled with 'log' to enhance readability. Statistical analysis by 1-way ANOVA/Kruskal-Wallis test followed by Tukey's/Dunn's multiple-comparisons post-hoc test **(B-D, E, G)**. Statistical analysis of zone-wise comparison of microviscosity was done by a Mann-Whitney test on each day **(E)**. Elastic and loss moduli are compared at 1Hz as an average across all mice, and statistical analysis is done by Kruskal-Wallis Test **(F)**. *p<0.05, **p<0.01, ***p<0.001, ****p<0.0001. N = 10-15 female mice.

B (0.08 ± 0.04 Pa and 0.2 ± 0.06 Pa, day 3 and 14, respectively) and T cell zones (0.15 ± 0.07 Pa and 0.2 ± 0.08 Pa, day 3 and 14, respectively) (**Fig. 6F**), though this was not significant. Loss moduli were similar on day 3 (0.06 ± 0.02 Pa*s) and day 14 (0.1 ± 0.05 Pa*s) compared to untreated (0.07 ± 0.02 Pa) (**Fig. 6F**). Loss moduli were also similar at days 3 and 14 in B (0.06 ± 0.03 Pa and 0.1 ± 0.04 Pa, day 3 and 14, respectively) and T cell zones (0.07 ± 0.02 Pa and 0.1 ± 0.04 Pa, day 3 and 14, respectively) (**Fig. 6F**). Median pore size within the lymph node significantly increased from 800 nm in untreated to 1400 nm on day 3 (**Fig. 6G)**; this was true for both B (1300 nm in untreated to 1600 nm at day 3) and T (300 nm in untreated to 1200 nm at day 3) cell zones (**Fig. 6G)**. These patterns remained true one month ("long-term resolution") after the final LPS challenge. Median pore sizes within the lymph node were significantly increased from untreated (800 nm) to long-term resolution (1200 nm) (**Supp. Fig. S4A**), as well as in the B (1300 nm untreated to 1400 nm long-term) and T (300 nm untreated to 1100 nm long-term) cell zones (**Supp. Fig. S4A**). Elastic and loss moduli remained similar to untreated at long-term resolution both overall and in the B and T cell zones **(Supp. Fig. S4C)**.

DISCUSSION

Elucidating the role of the influence of biomechanical stimuli on immune cell behavior and function has been an area of active interest[37-39]. In this study, we examined the biomechanical properties of the lymph node, a central pillar involved in the coordination of immune response. Using MPT microrheology[30,31,36], a minimally invasive technique, we provide a comprehensive analysis of lymph node biomechanics (elastic/loss moduli, pore size, microviscosity) during homeostasis and over the course of acute and chronic inflammation, including at resolution. We found that biomechanics of B and T cell zones change independently of each other during acute inflammation, and that changes in biomechanical properties are sex dependent. Our work suggests

that restructuring may in part depend on changes in ECM composition, and that chronic inflammation does not cause the same differences in biomechanical response as acute inflammation.

Lipopolysaccharide (LPS) initiates a TLR-4 response, which resulted in a lymph node expansion-contraction cycle that lasted approximately 14 days. Lymph nodes increase in size as soon as 1 day post initial stimulus and reach an inflammation peak at day 3 after LPS stimulation. We observed that an initial increase in the pore size at day 1 compared to untreated counterparts matches prior observations that the inter-network spacing of the reticular network is increased during the initial phases of lymph node expansion[7,8,10,11,40]. Additionally, we also observed a decrease in loss and elastic moduli one day after injection, which is consistent with previous work suggesting that lymph nodes undergo a priming step during early phases of expansion, where network tension is reduced[6,8,10]. By peak inflammation (3 days post injection), lymph nodes are nearly doubled in size, on account of increased cellularity. Previous studies[4,5,7,9] have shown that lymphocyte influx plays a key role in lymph node swelling mechanics and that perturbing the entry of lymphocytes leads to both a lowered viscosity and lymph node volume[9]. Lymph node swelling is also associated with stretching of the reticular network and changes to FRC size[8,9,40]. We note the increased cellularity at day 3 corresponds to a decrease in pore size and the higher viscosity echoes trends reported earlier. A consequence of increased cellularity could be a decrease in interstitial fluid density within the lymph node, which coupled with reduced pore sizes, may result in altered cell migration patterns within the lymph node. Smaller pores reduce the ease of nuclear movement for migrating cells[42], which can have adverse effects on their survival[43,44] as they navigate through the complex lymph node microenvironment.

Quantifying the morphology—particularly the pore size or mesh spacing—of hydrogels

and hydrogel-like tissues has been a long-standing interest in tissue engineering, drug delivery, and the study of cell migration[62-66]. The pore size distribution significantly impacts the mechanical properties, such as elastic and loss moduli, of hydrogels and tissues. Therefore, precise determination of pore sizes has broad implications for a wide range of biomedical applications. In this study, we used two characterization methods (MPT and gap analysis) to characterize the pore size of lymph node tissue. We found the two methods gave us contrasting results, likely due to their direct (gap analysis) and indirect (MPT) nature of evaluation. Indirect evaluation methods, like MPT, are rapid and non-invasive. By leveraging individual particle diffusivities, they can capture the effects of local variations and constraints within tissues, such as those imposed by cells, the ECM, and other proteins on mesh spacing, details which cannot be captured by direct evaluation. However, the dependence on mathematical models and a priori assumptions involved in microrheological measurements[36] may not fully reflect the complexity of the tissue structure. Conversely, gap analysis, which uses spaces within the lymph node reticular network (via podoplanin staining), can provide a more direct insight into both the pore size distribution and spatial arrangement in the tissue. While this method circumvents issues faced with MPT-based analyses, it has a limited field of view and requires averaging data over many thin sections to obtain an accurate representation of the tissue structure. This likely introduces errors due to image artefacts or non-uniform sampling. The differences in our results thereby highlight the need for more careful selection and accurate reporting of the technique(s) used for tissue pore size evaluation. We also observed a negative correlation between pore size and collagen III deposition, suggesting increased ECM deposition may be responsible for changes in tissue morphology, and consequently tissue biomechanics. Exploring the relative contributions of the ECM on lymph node biomechanics is a key area for subsequent investigation.

Our work also revealed that the B and T cell zones of the lymph node exhibit distinct restructuring patterns. While the B and T cell zones exhibit different trends in pore size, the ratio of B to T cell zone pore sizes shows an increasing trend over the course of an immune challenge, suggesting a higher degree of reorganization in the B cell zones. These data reflect similar patterns observed in other studies that highlight changes in the relative volume fractions of the B cell zone and T cell zone in the lymph node following adjuvant stimulation - there was a notable increase in the size of the B cell zone with a concurrent decrease in the T cell zone. Differences in restructuring may be due to the maturation of follicles to germinal centers at different time points. B cells undergo somatic hypermutation over time and these cellular changes may affect restructuring. The prevailing view is that the overall changes in lymph node structure were largely due to the reticular network in the T cell zone[9,13,15,45], but these findings indicate that the B cell zone may play a larger role than previously thought.

The prevalence of sex bias in immune cell counts and immune response between males and females is well documented[46-48]. Here, we demonstrated for the first time that biological sex also influences the mechanical properties and restructuring of lymph node tissue during acute inflammatory response. Lymph nodes in female mice exhibit higher elastic and loss moduli than lymph nodes from male mice over the course of immune response. Interestingly, 3 days post inflammatory stimulus, we observe a peak in elastic/loss moduli in female lymph nodes but a minima in male lymph nodes. This reversal of trends could be indicative of males and females exhibiting differing immune response rates to LPS, which may be influenced by sex hormones. Indeed, several clinical studies and in vitro models have demonstrated higher proinflammatory cytokine release[49-52] in males compared to females. Conversely, there is evidence to suggest that the influence of male sex hormones, androgens, may have an inhibitory effect[53,54], leading to sex-

based discrepancies and a diminished immune response in males. One study suggests that the TLR4 receptor, responsible for detection of LPS, may be regulated by testosterone. They found TLR4 expression on macrophages was reduced in the presence of testosterone in vitro, and surgical castration led to an increase in TLR4 expression and elevated inflammatory response in male mice[55]. Another study[56] demonstrated that androgens down regulated the number of skin-resident dendritic cells and lowered their migratory capacity to lymph nodes in male mice. While the effect of androgens may provide an explanation for our observations during lymph node expansion, additional research is needed to accurately assess the effect of sex hormones on lymph node biomechanics during the resolution phase of acute inflammation.

Disease states such as chronical inflammation, and even aging, have been shown to alter lymph node structure as well as impaired immune functions[17,57]. In aging, there is an increase in collagen deposition and a blurring of boundaries between B and T cell zones in the lymph nodes[18,58,59]. This suggests that aging may result in stiffer lymph node tissue environments and research has shown that viscoelasticity can modulate T cell functions, including expression of activation vs. memory markers[16]. Furthermore, aging appears to reduce T cell migration speed and linearity, which is also exacerbated in regions close to the extracellular matrix, suggesting that the biophysical environment surrounding T cells can affect their functions[17]. One hypothesis in aging is that the repeated inflammatory insults we experience throughout our lives cause permanent lymph node remodeling. We sought to mimic this by inducing chronic inflammation, but our data suggest that at least after one month of inflammation, there are minimal biophysical changes in the lymph nodes. However, our study may be limited by the length and type of inflammatory cues we used [67,68]. Remodeling of tissues in chronic inflammation may be slower than the time scales we observed; thus, future research investigating how different types of inflammation and duration of

chronic inflammatory stimuli impact lymph node biophysical properties would provide valuable insights and enhance the generalizability of our findings.

In summary, the role of biomechanics is heavily understudied in the context of immune responses, particularly in the lymph nodes. This study investigated for the first time how the biomechanics of the lymph node are altered during acute and one-month long inflammation and highlights the vital role of both the reticular network and lymph node architecture in modulating lymph node biophysical properties over the course of an acute inflammatory response. It also sheds light on the role of biological sex on lymph node biomechanics, providing an additional complexity to known sex differences in immune responses. Our work provides new insights into structure-function relationships in the lymph node and underscores the growing importance of tissue mechanics in understanding immune response.

MATERIALS AND METHODS

Animal work

Female and male C57BL/6 mice, 6-10 weeks old were intradermally injected with 10µg of LPS (Invivogen) to stimulate the right inguinal skin draining lymph node. Mice were euthanized by CO_2 inhalation 1, 3, 5, 7, or 14 days after injection. lymph nodes were collected and any fat surrounding the tissue was removed. Tissues were then placed in cold 1X PBS with 2% fetal bovine serum (FBS, ThermoFisher). All animal work was approved by the Institutional Animal Care and Use Committee at the University of Maryland, College Park.

Flow cytometry

After intradermal injection with LPS, inguinal lymph nodes were harvested for flow cytometry analysis. A single cell suspension was collected by pushing lymph nodes through a 70

μm cell strainer and then resuspended in RPMI (ThermoFisher) supplemented with 10% FBS (ThermoFisher), 1× l-glutamine (Corning), 50 U mL^{-1}Pen/Strep (Sigma), 50 μM beta-mercaptoethanol (ThermoFisher), 1 mM sodium pyruvate (ThermoFisher), 1× nonessential amino acids (Fisher Scientific), and 20 mM HEPES (GE Healthcare). Single cell suspensions were stained for viability (live/dead), B cells (B220+), total T cells (CD3+), helper T cells (CD4+), and cytotoxic T cells (CD8+). Stained cell suspensions were analyzed using flow cytometry with a BD FACS Celesta and FlowJo Version 10.

Tissue slicing

Slicing of lymph nodes was done as previously described[30,32]. Briefly, tissues were embedded in a 6% w/v low melting agarose (Thomas Scientific) and left to solidify. Once the gel was solidified, tissues were punched out using a 10 mm biopsy punch (Robbins Instruments). Gel pieces were placed on the sample tray of a Leica VT1000s vibratome (speed of 3.9 mm/s, frequency of 0.3 Hz, and amplitude of 0.6 mm) and sliced 300 μm thick. Slices were collected using a brush and placed into RPMI (ThermoFisher) supplemented with 10% FBS (ThermoFisher), 1× l-glutamine (Corning), 50 U mL^{-1}Pen/Strep (Sigma), 50 μM beta-mercaptoethanol (ThermoFisher), 1 mM sodium pyruvate (ThermoFisher), 1× nonessential amino acids (Fisher Scientific), and 20 mM HEPES (GE Healthcare). Lymph node slices were incubated at 37 °C with 5% CO_2 in media for at least 1 h prior to performing MPT.

Immunofluorescence staining

Slices were stained for B and T cell zones as previous described[30]. Briefly, lymph nodes were blocked with purified anti-mouse CD16/32 (BioLegend) and then stained for B cell or T cell zones using primary and secondary antibodies: anti-mouse CD45R/B220-AF647 (BioLegend), anti-collagen III (Proteintech), and donkey anti-rabbit 488 (BioLegend).

Nanoparticle formulation

500 nm polystyrene beads were densely coated in polyethylene glycol (PEG) using ethyl-3-(3-dimethylaminopropyl) carbodiimide and *N*-hydroxysuccinimide chemistry, as previously described[60]. Particles were diluted in deionized (DI) water at a 1:4 ratio and sonicated. 5 kDa or 40 kDa amine-terminated PEG (Creative PEGworks) were conjugated to the surface of 500 nm and 1 µm carboxylate-modified fluorescent polystyrene beads (Fluospheres™, ThermoFisher), respectively, using 0.02 mM EDC (Invitrogen) and 14 mM NHS (Sigma) dissolved in 200mM borate buffer (pH = 8.2). The reaction was allowed to proceed on a rotary shaker for at least 4 hours at room temperature. For maximum PEG coverage on 500 nm and 1 µm beads, 1.575 µmol of 5kDa PEG and 0.2175 µmol of 40kDa PEG were used, respectively. Particles were centrifuged for 10 minutes at 15000 x g and 12 minutes at 10000 x g for 500 nm and 1 µm particles, respectively, and washed 3 times using DI water. Particles were resuspended at 1% w/v in DI water and stored at 4ºC. Particle size and ζ-potential was characterized using dynamic light scattering (DLS) and phase analysis light scattering (PALS) (Brookhaven Instruments).

Multiple particle tracking (MPT) analysis

Up to 2µL of a 1:1000 nanoparticle dilution was pipetted on top of each lymph node slice. A coverslip was placed on top of the slice. A ZEISS Axioscope 5 microscope with 63X objective using ZEISS software (ZEN lite) was used to capture videos at a temporal resolution of 30 ms for 6 seconds. 4 slices were collected from each node, with 3 videos collected from each slice (representing the B cell zone, T cell zone, and a random zone). Averages for the 'overall node' are computed from data collected from all 4 slices across all zones (total of 12 videos per lymph node). Averages for the B and T cell zones ignore all videos collected in the random zone. Ensemble averaged mean square displacement (MSD) was calculated from nanoparticle trajectory using

MATLAB[61] with at least 50 particles per video. MSD was calculated using $\Delta r^2(\tau) = [x\ (t+\tau) - x(t)]^2 + [y\ (t+\tau) - y(t)]^2$. The MSD values were then used to extrapolate the microrheological properties of the tissue using the generalized Stokes-Einstein relation[33], defined as $\tilde{G}(s) = \frac{k_B T}{\pi a s \langle \Delta r^2(s) \rangle}$, where k_BT is the thermal energy, a is the particle radius, and s is the complex Laplace frequency. Using the frequency-dependent, complex modulus equation, $G^*(\omega) = G'(\omega) + iG''(\omega)$, where s is substituted with $i\omega$, we can solve for the elastic and loss moduli. The complex microviscosity (η^*) can be calculated as $\eta^* = G^*(\omega)/\omega$, where ω is the frequency. Comparisons of loss and elastic moduli were made at a value of 1Hz, in line with standard rheological measurements. The pore size (ξ) is estimated from the MSD[62] using the equation $\xi = \sqrt{MSD} + a$, where a is the particle radius. Pore size data represent all pore sizes collected from all particles in each slice.

Gap analysis

Lymph nodes were embedded in optimal cutting temperature compound (Tissue-Tek O.C.T. Compound) and flash frozen via liquid nitrogen. Tissues were stored at -80°C until slicing. 10 μm thick slices were collected using a Leica CM1950 Cryostat. Tissues were then washed with 1x PBS to remove excess OCT and fixed with 2% paraformaldehyde (PFA) in 1x PBS for 5-15 minutes. Tissues were blocked with 0.5% w/v casein in 1x PBS. Slices were imaged using a FV3000 Laser Scanning Confocal Microscope (Olympus) with the following settings: 1.5x zoom with 1024x1024 pixel resolution. The tiling feature was used to create a stitched 3x3 image of the tissue. Z-stack images were captured with 10 slices, each separated by a 0.5-step interval. Images were analyzed using FIJI. The individual stacks were merged using the z-project function at standard deviation projection. Images were then processed using the gap analysis script[7]. Briefly,

images were resized by a factor of 0.4. They were then converted into binary based on a pixel intensity threshold of 0.001. The largest circles possible were fitted into the gaps so that the circles were not overlapping with each other. Circle radii were collected in pixels and converted to μm based on the microscope resolution using the gap analysis script.

Statistics

All statistical analyses were performed using GraphPad Prism 10. P values ≤ 0.05 are considered significant. Sample sizes were either predetermined based on power analysis ($p=0.05$, $\alpha = 0.8$) guided by prior experience with similar experiments. In general, two-group comparisons were performed using two-tailed, unpaired Student's t-tests or their non-parametric equivalents depending on data distribution. For multiple group comparisons, one-way ANOVA with Tukey's multiple comparison test or a non-parametric Kruskal-Wallis test followed by Dunn's multiple comparisons test were conducted. Normality and homoscedasticity were evaluated prior to analysis to confirm the assumptions of the statistical tests applied. Figure legends include details of the statistical analyses performed for the figure dataset.

ACKNOWLEDGEMENTS

This work was supported by financial support from NIGMS MIRA 1R35GM142835-01 (KM, VS) and NIH HPI T32 (AR). All animal procedures were performed in accordance with the Guide for the Care and Use of Laboratory Animals and the American Veterinary Medical Association (AVMA) Guidelines for the Euthanasia of Animals and approved by the Institutional Animal Care and Use Committee at the University of Maryland, College Park. We would like to thank Dr. Giuliano Scarcelli, Sachin Suresh, and Anoushka Dasgupta for their constructive discussions regarding the analysis.

REFERENCES

1. Schudel, A., Francis, D. M. & Thomas, S. N. Material design for lymph node drug delivery. *Nat Rev Mater* **4**, 415-428, doi:10.1038/s41578-019-0110-7 (2019).
2. Li, L., Wu, J., Abdi, R., Jewell, C. M. & Bromberg, J. S. Lymph node fibroblastic reticular cells steer immune responses. *Trends Immunol.* **42**, 723-734, doi:10.1016/j.it.2021.06.006 (2021).
3. Fletcher, A. L., Acton, S. E. & Knoblich, K. Lymph node fibroblastic reticular cells in health and disease. *Nat. Rev. Immunol.* **15**, 350-361, doi:10.1038/nri3846 (2015).
4. Yang, C.-Y. *et al.* Trapping of naive lymphocytes triggers rapid growth and remodeling of the fibroblast network in reactive murine lymph nodes. *Proceedings of the National Academy of Sciences* **111**, E109-E118, doi:doi:10.1073/pnas.1312585111 (2014).
5. Zhu, M. & Fu, Y.-X. The role of core TNF/LIGHT family members in lymph node homeostasis and remodeling. *Immunol. Rev.* **244**, 75-84, doi:https://doi.org/10.1111/j.1600-065X.2011.01061.x (2011).
6. Astarita, J. L. *et al.* The CLEC-2-podoplanin axis controls the contractility of fibroblastic reticular cells and lymph node microarchitecture. *Nat. Immunol.* **16**, 75-84, doi:10.1038/ni.3035 (2015).
7. Acton, S. E. *et al.* Dendritic cells control fibroblastic reticular network tension and lymph node expansion. *Nature* **514**, 498-502, doi:10.1038/nature13814 (2014).
8. Horsnell, H. L. *et al.* Lymph node homeostasis and adaptation to immune challenge resolved by fibroblast network mechanics. *Nat. Immunol.* **23**, 1169-1182, doi:10.1038/s41590-022-01272-5 (2022).
9. Assen, F. P. *et al.* Multitier mechanics control stromal adaptations in the swelling lymph node. *Nat. Immunol.* **23**, 1246-1255, doi:10.1038/s41590-022-01257-4 (2022).
10. Alapan, Y. & Thomas, S. N. Mechanics drive lymph node expansion. *Nat. Immunol.* **23**, 1139-1141, doi:10.1038/s41590-022-01277-0 (2022).
11. Martinez, V. G. *et al.* Fibroblastic Reticular Cells Control Conduit Matrix Deposition during Lymph Node Expansion. *Cell Rep.* **29**, 2810-2822.e2815, doi:https://doi.org/10.1016/j.celrep.2019.10.103 (2019).
12. Textor, J., Mandl, J. N. & de Boer, R. J. The Reticular Cell Network: A Robust Backbone for Immune Responses. *PLoS Biol.* **14**, e2000827, doi:10.1371/journal.pbio.2000827 (2016).
13. Bajénoff, M. *et al.* Stromal cell networks regulate lymphocyte entry, migration, and territoriality in lymph nodes. *Immunity* **25**, 989-1001, doi:10.1016/j.immuni.2006.10.011 (2006).
14. Lämmermann, T. & Sixt, M. The microanatomy of T-cell responses. *Immunol. Rev.* **221**, 26-43, doi:https://doi.org/10.1111/j.1600-065X.2008.00592.x (2008).
15. Roozendaal, R., Mebius, R. E. & Kraal, G. The conduit system of the lymph node. *Int. Immunol.* **20**, 1483-1487, doi:10.1093/intimm/dxn110 (2008).
16. Adu-Berchie, K. *et al.* Generation of functionally distinct T-cell populations by altering the viscoelasticity of their extracellular matrix. *Nat Biomed Eng* **7**, 1374-1391, doi:10.1038/s41551-023-01052-y (2023).
17. Kwok, T. *et al.* Age-Associated Changes to Lymph Node Fibroblastic Reticular Cells. *Frontiers in Aging* **3**, doi:10.3389/fragi.2022.838943 (2022).
18. Sonar, S. A. *et al.* Early age–related atrophy of cutaneous lymph nodes precipitates an early

functional decline in skin immunity in mice with aging. *Proceedings of the National Academy of Sciences* **119**, e2121028119, doi:10.1073/pnas.2121028119 (2022).
19. Chaudhuri, O., Cooper-White, J., Janmey, P. A., Mooney, D. J. & Shenoy, V. B. Effects of extracellular matrix viscoelasticity on cellular behaviour. *Nature* **584**, 535-546, doi:10.1038/s41586-020-2612-2 (2020).
20. Batzdorf, C. S. *et al.* Sexual Dimorphism in Extracellular Matrix Composition and Viscoelasticity of the Healthy and Inflamed Mouse Brain. *Biology (Basel)* **11**, doi:10.3390/biology11020230 (2022).
21. Simon, L. R., Scott, A. J., Figueroa Rios, L., Zembles, J. & Masters, K. S. Cellular-scale sex differences in extracellular matrix remodeling by valvular interstitial cells. *Heart Vessels* **38**, 122-130, doi:10.1007/s00380-022-02164-2 (2023).
22. Guo, J. *et al.* Brain maturation is associated with increasing tissue stiffness and decreasing tissue fluidity. *Acta Biomater.* **99**, 433-442, doi:10.1016/j.actbio.2019.08.036 (2019).
23. Hernandez, P. A. *et al.* Sexual Dimorphism in the Extracellular and Pericellular Matrix of Articular Cartilage. *Cartilage* **13**, 19476035221121792, doi:10.1177/19476035221121792 (2022).
24. Ricarte, R. G. & Shanbhag, S. A tutorial review of linear rheology for polymer chemists: basics and best practices for covalent adaptable networks. *Polymer Chemistry* **15**, 815-846, doi:10.1039/D3PY01367G (2024).
25. Cho, D. H., Aguayo, S. & Cartagena-Rivera, A. X. Atomic force microscopy-mediated mechanobiological profiling of complex human tissues. *Biomaterials* **303**, 122389, doi:https://doi.org/10.1016/j.biomaterials.2023.122389 (2023).
26. Krieg, M. *et al.* Atomic force microscopy-based mechanobiology. *Nature Reviews Physics* **1**, doi:10.1038/s42254-018-0001-7 (2018).
27. Fonta, C. M. *et al.* Fibronectin fibers are highly tensed in healthy organs in contrast to tumors and virus-infected lymph nodes. *Matrix Biol Plus* **8**, 100046, doi:10.1016/j.mbplus.2020.100046 (2020).
28. Lobov, G. I. & Pan'kova, M. N. Mechanical Properties of Lymph Node Capsule. *Bull. Exp. Biol. Med.* **151**, 5-8, doi:10.1007/s10517-011-1246-7 (2011).
29. Najibi, A. J. *et al.* Lymph node expansion predicts magnitude of vaccine immune response. *bioRxiv*, 2022.2010.2025.513749, doi:10.1101/2022.10.25.513749 (2022).
30. Ramirez, A., Merwitz, B., Lee, H., Vaughan, E. & Maisel, K. Multiple particle tracking (MPT) using PEGylated nanoparticles reveals heterogeneity within murine lymph nodes and between lymph nodes at different locations. *Biomater Sci* **10**, 6992-7003, doi:10.1039/d2bm00816e (2022).
31. Lee, B., Cheema, Y., Bader, S. & Duncan, G. *Shaping nanoparticle diffusion through biological barriers to drug delivery*. (2021).
32. Belanger, M. C. *et al.* Acute Lymph Node Slices Are a Functional Model System to Study Immunity Ex Vivo. *ACS Pharmacology & Translational Science* **4**, 128-142, doi:10.1021/acsptsci.0c00143 (2021).
33. Mason, T. G. & Weitz, D. A. Optical Measurements of Frequency-Dependent Linear Viscoelastic Moduli of Complex Fluids. *Phys. Rev. Lett.* **74**, 1250-1253, doi:10.1103/PhysRevLett.74.1250 (1995).
34. Ensign, L. M. *et al.* Ex Vivo Characterization of Particle Transport in Mucus Secretions Coating Freshly Excised Mucosal Tissues. *Mol. Pharm.* **10**, 2176-2182, doi:10.1021/mp400087y (2013).

35. McCright, J., Skeen, C., Yarmovsky, J. & Maisel, K. Nanoparticles with dense poly(ethylene glycol) coatings with near neutral charge are maximally transported across lymphatics and to the lymph nodes. *Acta Biomater.*, doi:https://doi.org/10.1016/j.actbio.2022.03.054 (2022).
36. McGlynn, J. A., Wu, N. & Schultz, K. M. Multiple particle tracking microrheological characterization: Fundamentals, emerging techniques and applications. *Journal of Applied Physics* **127**, 201101, doi:10.1063/5.0006122 (2020).
37. Du, H. *et al.* Tuning immunity through tissue mechanotransduction. *Nature Reviews Immunology* **23**, 174-188, doi:10.1038/s41577-022-00761-w (2023).
38. Huse, M. Mechanical forces in the immune system. *Nat. Rev. Immunol.* **17**, 679-690, doi:10.1038/nri.2017.74 (2017).
39. Gunasinghe, S. D., Peres, N. G., Goyette, J. & Gaus, K. Biomechanics of T Cell Dysfunctions in Chronic Diseases. *Front. Immunol.* **12**, doi:10.3389/fimmu.2021.600829 (2021).
40. Link, A. *et al.* Fibroblastic reticular cells in lymph nodes regulate the homeostasis of naive T cells. *Nat. Immunol.* **8**, 1255-1265, doi:10.1038/ni1513 (2007).
41. Kumar, V. *et al.* A dendritic-cell-stromal axis maintains immune responses in lymph nodes. *Immunity* **42**, 719-730, doi:10.1016/j.immuni.2015.03.015 (2015).
42. Yamada, K. M. & Sixt, M. Mechanisms of 3D cell migration. *Nature Reviews Molecular Cell Biology* **20**, 738-752, doi:10.1038/s41580-019-0172-9 (2019).
43. Swift, J. *et al.* Nuclear lamin-A scales with tissue stiffness and enhances matrix-directed differentiation. *Science* **341**, 1240104, doi:10.1126/science.1240104 (2013).
44. Harada, T. *et al.* Nuclear lamin stiffness is a barrier to 3D migration, but softness can limit survival. *J. Cell Biol.* **204**, 669-682, doi:10.1083/jcb.201308029 (2014).
45. Song, J. *et al.* The extracellular matrix of lymph node reticular fibres modulates follicle border interactions and germinal centre formation. *iScience* **26**, 106753, doi:10.1016/j.isci.2023.106753 (2023).
46. Klein, S. L. & Flanagan, K. L. Sex differences in immune responses. *Nature Reviews Immunology* **16**, 626-638, doi:10.1038/nri.2016.90 (2016).
47. Schafer, J. M. *et al.* Sex-biased adaptive immune regulation in cancer development and therapy. *iScience* **25**, 104717, doi:10.1016/j.isci.2022.104717 (2022).
48. Takahashi, T. *et al.* Sex differences in immune responses that underlie COVID-19 disease outcomes. *Nature* **588**, 315-320, doi:10.1038/s41586-020-2700-3 (2020).
49. Aomatsu, M., Kato, T., Kasahara, E. & Kitagawa, S. Gender difference in tumor necrosis factor-α production in human neutrophils stimulated by lipopolysaccharide and interferon-γ. *Biochem. Biophys. Res. Commun.* **441**, 220-225, doi:10.1016/j.bbrc.2013.10.042 (2013).
50. Asai, K. *et al.* Gender differences in cytokine secretion by human peripheral blood mononuclear cells: role of estrogen in modulating LPS-induced cytokine secretion in an ex vivo septic model. *Shock* **16**, 340-343, doi:10.1097/00024382-200116050-00003 (2001).
51. Campesi, I., Montella, A. & Franconi, F. Human monocytes respond to lipopolysaccharide (LPS) stimulation in a sex-dependent manner. *J. Cell. Physiol.* **237**, 580-588, doi:10.1002/jcp.30503 (2022).
52. Aulock, S. V. *et al.* Gender difference in cytokine secretion on immune stimulation with LPS and LTA. *J. Interferon Cytokine Res.* **26**, 887-892, doi:10.1089/jir.2006.26.887 (2006).
53. Musabak, U. *et al.* Gonadotropin treatment restores in vitro interleukin-1beta and tumour

necrosis factor-alpha production by stimulated peripheral blood mononuclear cells from patients with idiopathic hypogonadotropic hypogonadism. *Clin. Exp. Immunol.* **132**, 265-270, doi:10.1046/j.1365-2249.2003.02141.x (2003).

54. D'Agostino, P. *et al.* Sex hormones modulate inflammatory mediators produced by macrophages. *Ann. N. Y. Acad. Sci.* **876**, 426-429, doi:10.1111/j.1749-6632.1999.tb07667.x (1999).
55. Rettew, J. A., Huet-Hudson, Y. M. & Marriott, I. Testosterone reduces macrophage expression in the mouse of toll-like receptor 4, a trigger for inflammation and innate immunity. *Biol. Reprod.* **78**, 432-437, doi:10.1095/biolreprod.107.063545 (2008).
56. Chi, L. *et al.* Sexual dimorphism in skin immunity is mediated by an androgen-ILC2-dendritic cell axis. *Science* **384**, eadk6200, doi:10.1126/science.adk6200 (2024).
57. Gubbels Bupp, M. R. Sex, the aging immune system, and chronic disease. *Cell. Immunol.* **294**, 102-110, doi:https://doi.org/10.1016/j.cellimm.2015.02.002 (2015).
58. Nikolich-Žugich, J. The twilight of immunity: emerging concepts in aging of the immune system. *Nat. Immunol.* **19**, 10-19, doi:10.1038/s41590-017-0006-x (2018).
59. Cakala-Jakimowicz, M., Kolodziej-Wojnar, P. & Puzianowska-Kuznicka, M. Aging-Related Cellular, Structural and Functional Changes in the Lymph Nodes: A Significant Component of Immunosenescence? An Overview. *Cells* **10**, 3148 (2021).
60. Nance, E. A. *et al.* A Dense Poly(Ethylene Glycol) Coating Improves Penetration of Large Polymeric Nanoparticles Within Brain Tissue. *Sci. Transl. Med.* **4**, 149ra119-149ra119, doi:10.1126/scitranslmed.3003594 (2012).
61. Schuster, B. S., Suk, J. S., Woodworth, G. F. & Hanes, J. Nanoparticle diffusion in respiratory mucus from humans without lung disease. *Biomaterials* **34**, 3439-3446,://doi.org/10.1016/j.biomaterials.2013.01.064 (2013).
62. Shin, J. H., Gardel, M. L., Mahadevan, L., Matsudaira, P. & Weitz, D. A. Relating microstructure to rheology of a bundled and cross-linked F-actin network in vitro. *Proc. Natl. Acad. Sci. U. S. A.* **101**, 9636-9641, doi:10.1073/pnas.0308733101 (2004).
63. Cabral, Jaydee, and Stephen Carl Moratti. "Hydrogels for biomedical applications." *Future medicinal chemistry* vol. 3,15 (2011): 1877-88. doi:10.4155/fmc.11.134
64. Q. L. Loh and C. Choong, Three-dimensional scaffolds for tissue engineering applications: role of porosity and pore size, Tissue Eng., Part B, 2013, 19(6), 485–502.
65. Hoffman AS. Hydrogels for biomedical applications. *Adv Drug Deliv Rev*. 2002;54(1):3-12
66. Leal-Egaña, Aldo et al. "Determination of pore size distribution at the cell-hydrogel interface." *Journal of nanobiotechnology* vol. 9 24. 27 May. 2011, doi:10.1186/1477-3155-9-24
67. Bernardette Martínez-Rizo, Abril et al. "Models in vivo and in vitro for the study of acute and chronic inflammatory activity: A comprehensive review." *International immunopharmacology* vol. 135 (2024): 112292. doi:10.1016/j.intimp.2024.112292
68. Rafiyan M, Sadeghmousavi S, Akbarzadeh M, Rezaei N. Experimental animal models of chronic inflammation. *Curr Res Immunol*. 2023;4:100063. Published 2023 Jun 11. doi:10.1016/j.crimmu.2023.100063

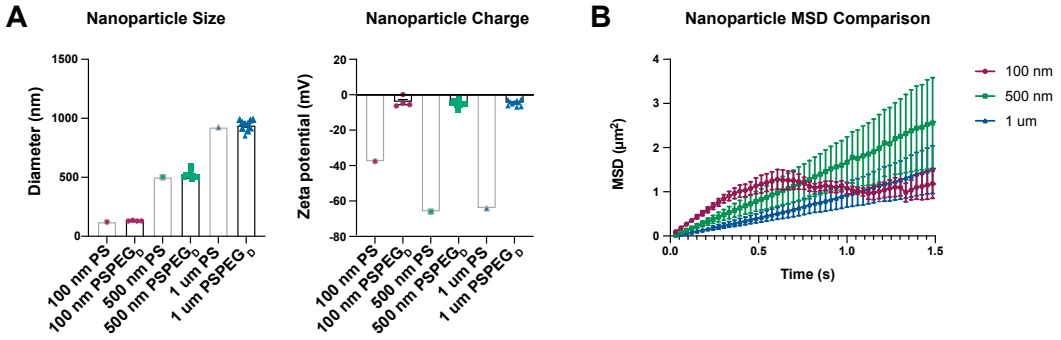

Supplementary Figure S1 *Nanoparticle characterization of PEGylated polystyrene beads* (A) Size and charge analyzed by dynamic light scattering (DLS) and phase analysis light scattering (PALS). (B) Mean square displacement of PSPEG$_D$ 100nm, 500nm and 1μm polystyrene beads. All values shown are mean ± SEM.

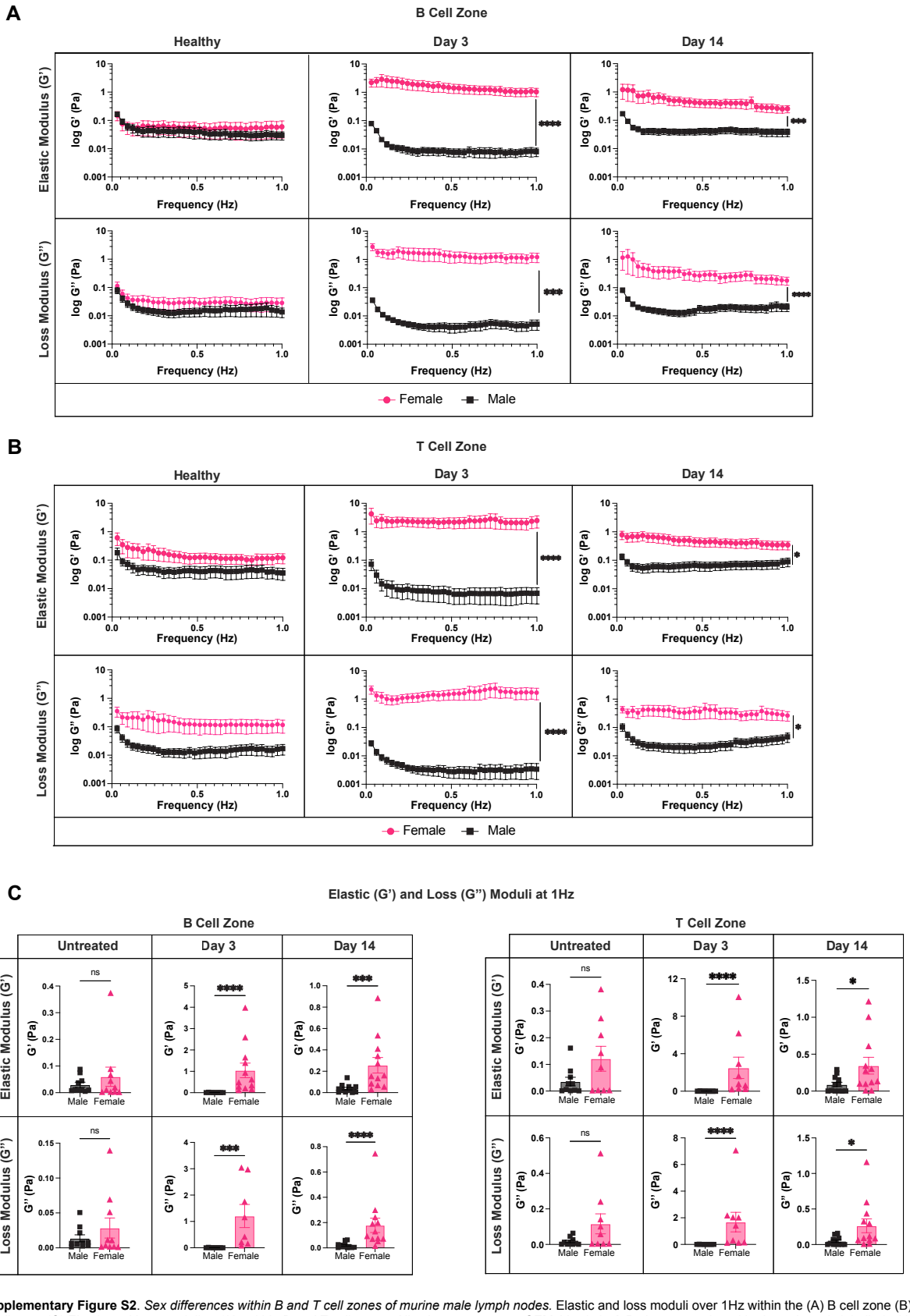

Supplementary Figure S2. *Sex differences within B and T cell zones of murine male lymph nodes.* Elastic and loss moduli over 1Hz within the (A) B cell zone (B) T cell zone (C) Elastic and loss moduli at 1Hz within B and T cell zones. All values are mean ± SEM. Y-axis in **A,B** shown on a logarithmic scale, axis labelled with 'log' to enhance readability. Elastic and loss moduli are compared at 1Hz as an average across all mice, and statistical analysis is done by Mann-Whitney test(**A-C**). Significance values are denoted on **A,B** for representation. *p<0.05, **p<0.01, ***p<0.001, ****p<0.0001, ns p≥0.05. N=8-12 male and female mice.

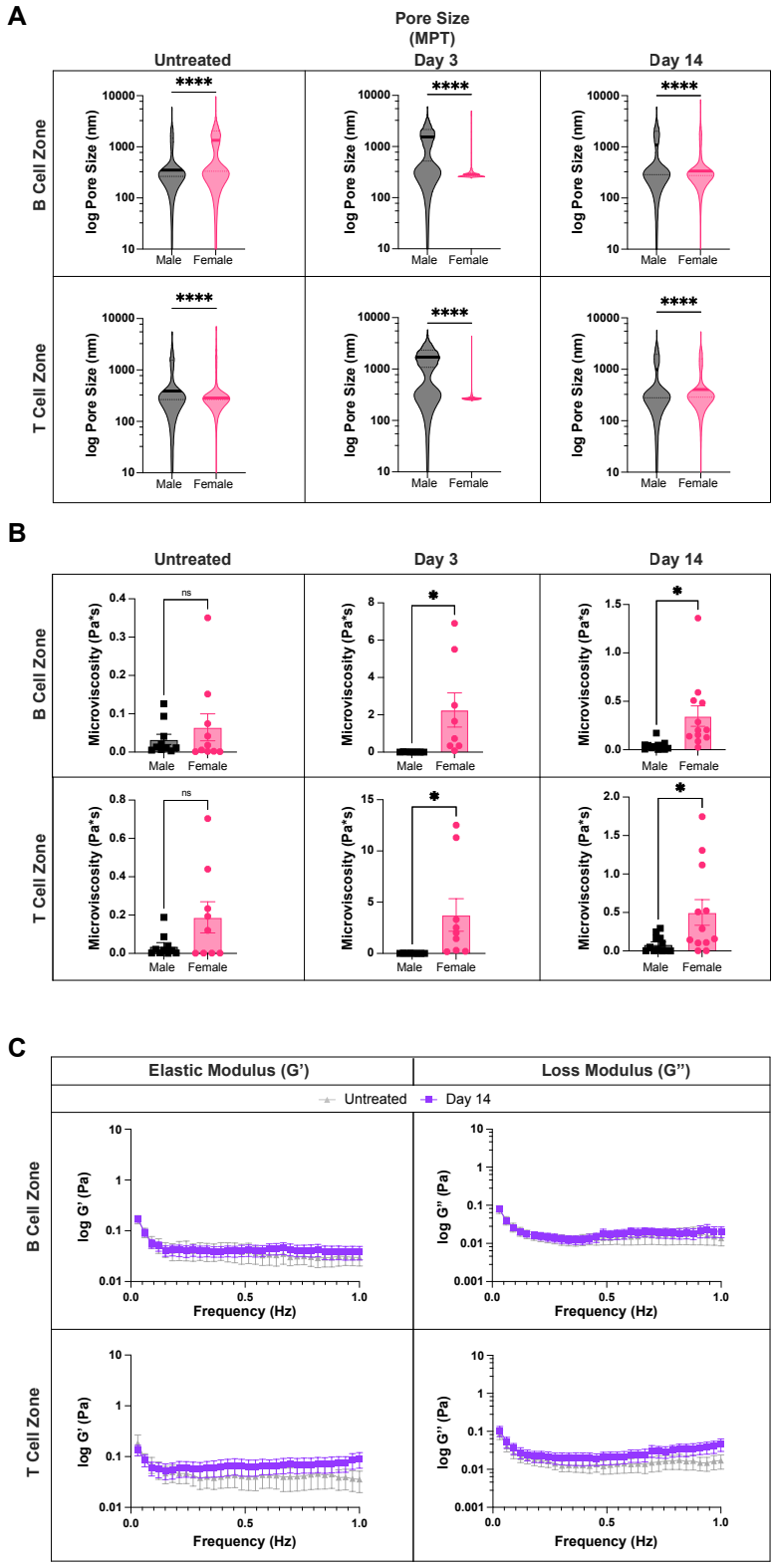

Supplementary Figure S3 *Sex differences within B and T cell zones* (A) Pore sizes(by MPT) in B and T cell zones (B) Microviscosity in B and T cell zones (C) Elastic and loss moduli over 1Hz in male untreated and day 14 lymph nodes. All values are mean ± SEM. Y-axis in **A,C** shown on a logarithmic scale, axis labelled with 'log' to enhance readability. Statistical analyses of microviscosity data done by Mann-Whitney test **(A).** Elastic and loss moduli are compared at 1Hz as an average across all mice, and statistical analysis is done by Mann-Whitney test **(C).** *p<0.05, **p<0.01, ***p<0.001, ****p<0.0001, ns p≥0.05. N=8-12 male and female mice.

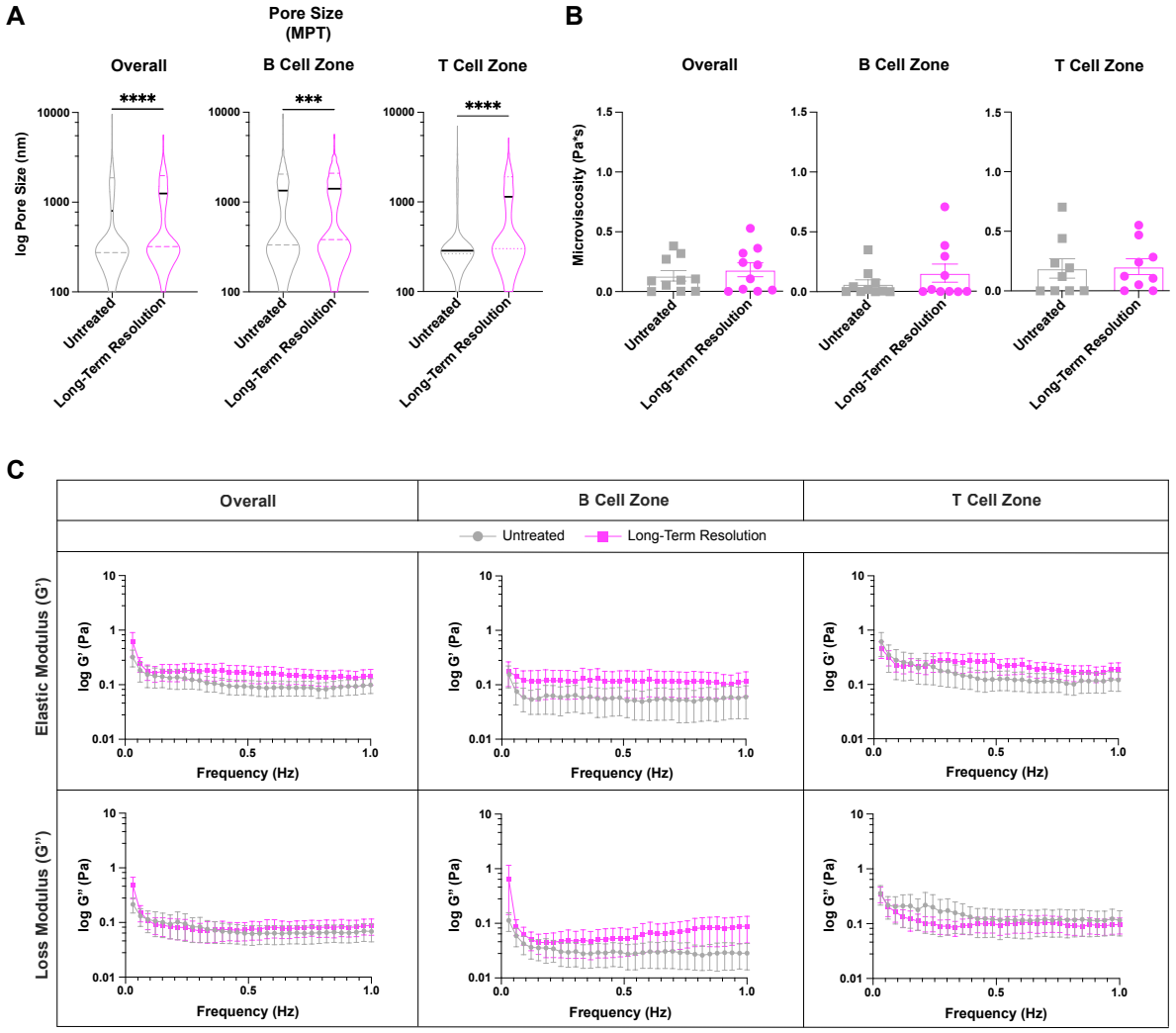

Supplementary Figure S4 *Chronically inflammed lymph nodes left to recover for 4 weeks, exhibit similar biomechanics to untreated lymph nodes* (A) Pore sizes (by MPT) in the overall lymph node and in the B and T cell zones (B) in the overall lymph node and in the B and T cell zones (C) Elastic and loss moduli over 1Hz in untreated and lymph nodes after long-term resolution. All values are mean ± SEM. Y-axis in **A,C** shown on a logarithmic scale, axis labelled with 'log' to enhance readability. Statistical analyses of microviscosity data done by Mann-Whitney test **(A,B).** Elastic and loss moduli are compared at 1Hz as an average across all mice, and statistical analysis is done by Mann-Whitney test **(C).** *p<0.05, **p<0.01, ***p<0.001, ****p<0.0001, ns p≥0.05. N=10-15 female mice.